PCCP

Accepted Manuscript

ROYAL SOCIETY OF CHEMISTRY

www.rsc.org/pccp

Significant enhancement of optical absorption through nano-structuring of copper based oxide semiconductors: Possible future materials for solar energy applications

Anagh Bhaumik[a], Austin M Shearin[a], Rishi Patel[a], and Kartik Ghosh*[a]
[a]Department of Physics, Astronomy and Materials Science and Center for Applied Science and Engineering, Missouri State University, Springfield, MO 65897, USA.
E-mail: *KartikGhosh@MissouriState.edu*

Table of contents entry

An excellent optical absorption coefficient-twice that of Si is successfully achieved in nanostructured phase mixture of copper based oxide semiconductor.

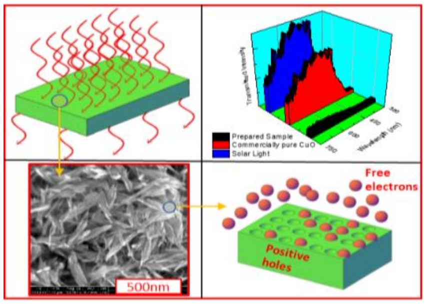

The optical absorption coefficient is a crucial parameter in determining solar cell efficiency under operational conditions. It is well-known that inorganic nano crystals are a benchmark model for solar cell nanotechnology, given that the tunability of optical properties and stabilization of specific phases are uniquely possible at the nanoscale. A hydrothermal method was employed to fabricate nanostructured copper oxides where the shape, size and phase were tailored by altering the growth parameters, namely the base media used, the reaction temperature, and the reaction time. The nano crystalline structures, phases, morphology, molecular vibrational modes, and optical properties were investigated using X-Ray diffraction (XRD), scanning electron microscopy (SEM), Raman spectroscopy, photoluminescence (PL), and UV-vis spectroscopy. A significantly large optical absorption coefficient, of the order of twice that of Si in the visible range, was observed in a particular phase mixture of nanostructured copper oxide. An optical absorption coefficient of 7.05E+5 cm^{-1} at 525nm was observed in a particular nanostructured phase mixture of copper oxides which is appreciably larger than commercially pure CuO (1.19E+5 cm^{-1}) and Si (1.72E+5 cm^{-1}). A possible mechanism of formation of phase mixtures and morphology of copper oxides has also been discussed, which opens a roadmap in synthesis of similar morphology nanostructures for efficient solar cells.

Introduction

The numerous detrimental aspects of fossil-fuel energy sources evolve a greater need to explore alternative sources of energy. Solar cell technology is one of such being state-of-art is an excellent source of renewable energy. The physics of semiconductor materials used in solar cell technology is predominantly governed by their energy band gap and optical properties. When sunlight strikes the surface of a PV cell, its absorption depends on the absorption coefficient and energy band gap of the semiconductor materials used in the solar cell. [1,2] The absorption factor of a PV cell is defined as the fraction of incident solar irradiance that is absorbed by the cell. An increase in solar absorption coefficient increases the electron-hole pair generation rate, which forms the backbone for a more efficient solar cell. Considerable efforts have been made to develop novel materials that absorb better at long wavelengths, so far with little success.[3,4] One such option to improve the absorption of red and near infrared light is by increasing the nanoparticle film thickness to improve the optical density; however this leads to exceeding the electron diffusion length through the nanoparticle network.[5] Therefore unique materials with a large optical absorption coefficient must be developed to overcome these issues.

The use of nanostructured materials represents a general approach to reduce both cost and size and to improve efficiency in photovoltaic cells.[6,7] The physical mechanism underlying high external quantum efficiencies for photoluminescence in low dimensional materials is mainly that of the quantum confinement of excitons in a nanometer-scale crystalline structure.[8,9] As photons are absorbed by the material and charge carriers are produced, the average diffusion time (τ) from the bulk of the material to the surface has been shown to follow equation (1):

$$\tau = \frac{r^2}{\pi^2} D \qquad (1)$$

Where, r is the grain radius and D is the diffusion coefficient of the material.[1] With a decrease of grain radius, the diffusion time for these charge carriers is reduced and thus there is less of a chance for recombination thereby increasing the efficiency of the solar cell.

Stringent control over the morphology of the nanomaterial itself has been shown to change the optical properties of a material.[10] For example, bulk copper oxide has a band gap of 2.17 eV, whereas nanocrystalline thin film and nanowires of copper oxide have band gaps of 2.06 eV and 2.69 eV, respectively.[1] Superior optical activity of metal oxide nano flowers have also been reported.[11] The morphology associated with both the particle network and the inter particle contact area also dictates solar activities.[12,13] Band gap engineering for better optical properties is being widely used for metal oxides by the process of doping[14], and mixed oxide synthesis.[15] The thrust to synthesize nanostructures with well-defined geometrical shapes and organize them as 2- and 3-dimensional assemblies have further expanded the possibility of developing new strategies for light energy conversion.[16,17]

The dominance of Si solar cells is now being challenged by new generations of photovoltaic cells.[18] Copper oxide was one of the earliest materials studied for solar cell applications due to its semiconductor properties,[19] but other materials such as silicon and germanium were further developed since they more closely approached Shockley-Quisser limit.[1] Copper oxide compounds provide a unique possibility to tune the optical and electronic properties from insulating to metallic conduction, from band gap energies of 2.1eV to the infrared at 1.4eV, i.e. right into the middle of the maximum efficiency for solar-cell applications. Cupric oxide (CuO) and Cuprous oxide (Cu_2O) are being widely used as a p-type semiconductor for designing solar cells. [20,21] Thus, there will be a considerable change in the optical properties with the change in phase percentage, morphology and size of room temperature stable copper oxides. We report an excellent optical solar absorption characteristic (two times that of Si in the visible range) in a particular phase percentage of hydrothermally prepared nanostructured mixture of CuO and Cu_2O.

Results and discussion

Synthesis of copper oxide composite nanostructures

Phase mixtures of copper oxide nanostructures were synthesized by hydrothermal process for 15 hours at different reaction temperatures. Different bases (KOH, NH_4OH, and NaOH) were reacted with copper sulphate pentahydrate ($CuSO_4.5H_2O$) to form nanostructures of copper oxide. In order to investigate the growth mechanism and the action of ethylene glycol (EG), the experiments were carried out with the addition of 10ml EG. The obtained samples were characterized using X-ray powder diffraction (Bruker, D8 Discover) θ–2θ scan with CuK_α (λ=1.5405Å); Rietveld analysis was done using Diffrac *plus* Topas software. The morphology of as-prepared samples were characterized by Scanning electron microscopy (FEI Quanta 200S). The vibrational phonon modes of the resulting copper oxides were determined by Raman spectroscopy using a 532nm green laser (Horiba Labram Raman-PL). Photoluminescence measurements were carried out employing a 325nm UV laser using the abovementioned instrument. Absorption characteristics spectra were measured by Ocean Optics HR 4000 spectrometer in conjunction with Ocean Optics Spectra suite software. Details of the synthesis and characterization procedures have been provided in the experimental section.

Structural and physical properties

X-ray diffraction (XRD)

Powder XRD was carried out on all the copper oxide powder samples synthesized by hydrothermal process. The Rietveld analysis of XRD data for four selected copper oxide powder samples are shown in Figure 1. Samples A, B, C, and D represent copper oxides formed under varied reaction parameters and possess different optical absorption characteristics. The observed XRD pattern (black line) along with that of calculated (red line) using Rietveld analysis and difference (blue line) profile for the powder sample are shown in Figure 1. XRD data indicate that mixture of copper oxides are formed which crystallizes in space group symmetry of C12/c1 (monoclinic) and Pn-3m Z (cubic) for CuO and Cu_2O, respectively.

The crystal structure was extracted by Rietveld analysis and is represented in Figure 2. The calculated bond angles (a and b) along with the bond lengths (c) is tabulated in Table 1. The disappearance of higher angle XRD peaks in sample D can be accounted for higher degree of preferentially oriented planes of CuO. The calculated phase percentages of CuO and Cu_2O, size, strain, Cu-O-Cu, O-Cu-O bond angles, Cu-O bond lengths, and goodness of fit (GOF) are shown in Table 1 for samples prepared with different reaction parameters, accordingly to a decrease in solar absorption characteristics. Sample A shows the least deviation in bond angles and bond lengths from pure CuO.

A larger deviation in bond angles and bond lengths from the pure CuO results in weak or strained bonds. The energy of the weak bonds is higher and these bonds can easily break to form defects in the atomic network. Band tail states represent the energy states of electrons that form the strained bonds in the crystal network.[22] Increase in disorder and strained bonds increases the width of the tail states. The wave functions of the tail and defect states are localized within the structure and therefore these states are also referred to as localized states. The mobility of the charge carriers are least in these localized states.[23,24]The size, strain, bond angles, and bond length were calculated for CuO. The standard values of O-Cu-O/ Cu-O-Cu angles are 95.72^0 and 78.96^0, and bond length (Cu-O) is 1.961Å for pure CuO. [25]

The tail states act as trapping centres [26]and build up a space charge in a potential device, which acts as very effective recombination centres and affect in particular the lifetime of the charge carries, which is detrimental for a solar cell. Incorporation of sample A having least deviation in the cell parameters from the standard crystal structure can considerably increase the efficiency of solar cells. An interesting interdependence of bond angles with solar absorption characteristics can be found from bond angle calculations. Increased solar absorption activities can be related with an increase in O-Cu-O bond angle and a decrease in Cu-O-Cu bond angle where, the bond length seems to play a lesser role in the absorption properties. The change in bond angles is not too predominant when EG is being used as a modifier and reducer in the hydrothermal process, thus, introduction of EG plays a crucial role for better solar absorption properties. However, it should be noted that increased solar absorption should not only be accounted to minimal changes in the bond angle.

It can be concluded from Rietveld analysis that nanostructured copper oxide composite having phase percentage of 97.7:2.3 ($CuO:Cu_2O$) and possessing a minimal perturbation of bond angle from the standard crystal structure has excellent solar absorption properties, which can be utilized in fabricating solar cells.

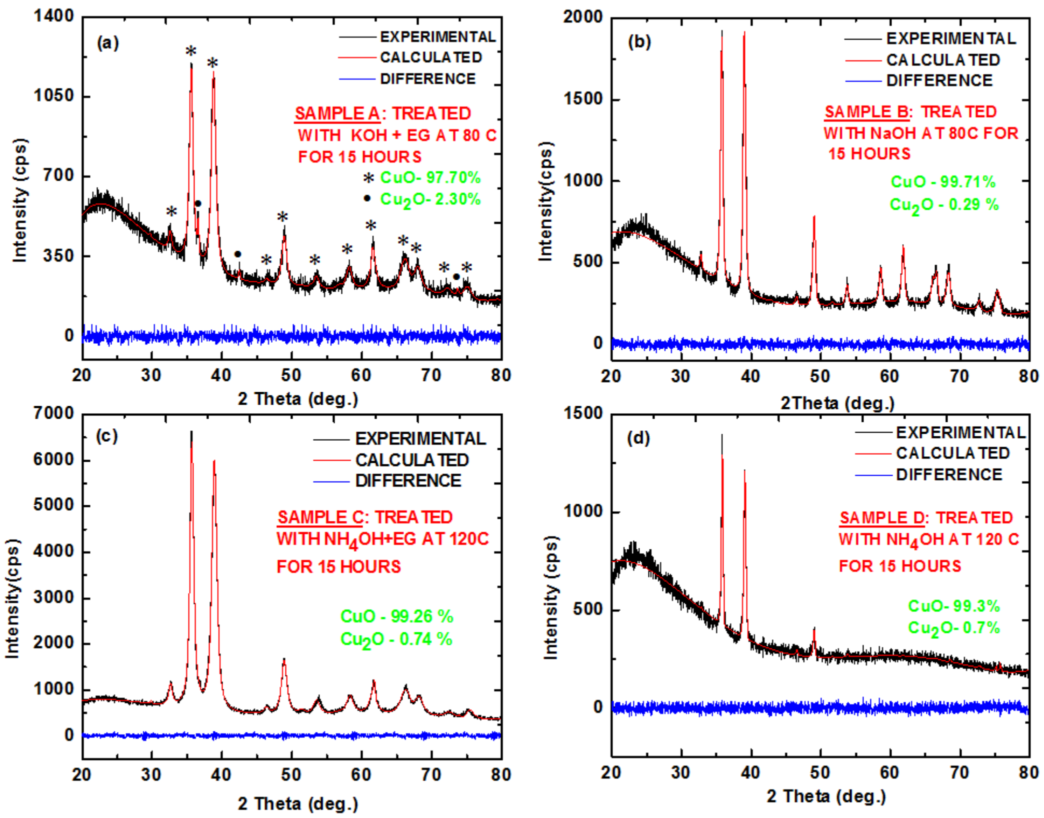

Fig. 1. Rietveld fitted XRD pattern of (a) Sample A, (b) Sample B, (c) Sample C, and (d) Sample D having different optical absorption properties. The observed XRD pattern (black line) along with that of calculated (red line) using Rietveld analysis and difference (blue line) profile for the powder sample are shown in the figure. XRD data indicate that mixture of copper oxides are formed which crystallizes in space group symmetry of C12/c1 (monoclinic) and Pn-3m Z (cubic) for CuO and Cu_2O.

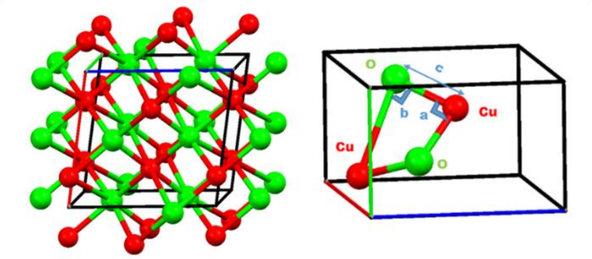

Fig. 2. Crystal structure of monoclinic CuO showing the measured bond angles and bond length, extracted from crystallographic information file (cif) by Rietveld analysis. The red balls represent Cu^{2+} and the green ones O^{2-}.

Raman spectroscopy

The Raman spectra of the four selective hydrothermally synthesized copper oxide powder samples (A, B, C, D) are shown in Figure 3. The Raman data was analyzed using Voigt peak fittings in Labspec 5 software. CuO belongs to the C^6_{2h} space group with two molecules per primitive cell.[7] There are nine zone-center optical phonon modes with symmetries $4A_u + 5B_u + A_g + 2B_g$; only three modes ($1A_g + 2B_g$) are Raman active.[27,28] The optical vibrational Raman active modes present in pure CuO are at 290 cm^{-1} (A_g), 340 cm^{-1} (B_{1g}), and 620 cm^{-1} (B_{2g}).[29,30] A likely reason for the weakness of the latter signal (B_{2g}) is the strong polarization dependence of this particular mode.[31]

Cu_2O crystallizes in a cubic structure of space group O^4_h (*Pn3m*).[32,33] It's primitive cell contains two Cu_2O units, i.e., six atoms, yielding 15 optical phonon modes in addition to the three acoustic phonon modes.[34,35] Vibrations belonging to the threefold degenerate T_{2g} symmetry are the only Raman active modes in this material. The A_{2u} and E_u modes are silent modes.[36] It is worth noting that the reported Raman spectra may vary significantly in the mode intensities and the number of observed modes. The reason for this is the instability of Cu_2O that leads to a variety of intrinsic defects and a tendency towards nonstoichiometry.[37] Additional effects due to different excitation conditions i.e., in resonance and off resonance with the excitonic transitions of Cu_2O, due to a dependence on the scattering geometry and polarization conditions, and due to the surface treatment of the samples also play a role, but are less significant.[38,39,40] Nonstoichiometry due to the formation of point defects such as vacancies, interstitials, or antisite defects has two major effects. On the one hand, the translational symmetry is broken and the corresponding selection rules no longer strictly hold, e.g., the point defects reduce the local symmetry such that the distinction between Raman-allowed and Raman-forbidden lattice vibrations diminishes.

Table 1. Table showing the phase percentages, size, strain, bond angles, bond lengths, goodness of fit, and optical absorption (%) at 525nm of hydrothermally synthesized copper oxide samples accordingly to the decrease in solar absorption properties. The standard values of O-Cu-O/ Cu-O-Cu angles are 95.72^0 and 78.96^0, and bond length (Cu-O) is 1.961Å for pure CuO.[25]

[a)] The values were calculated for CuO only.

Reagent used	Reaction parameter	CuO %/ Cu_2O%	Size (nm)[a)]	Strain [a)]	Bond angle O-Cu-O (a)/ Cu-O-Cu(b) [a)]	Bond length Cu-O(c) Å [a)]	Goodness of fit (gof)	Absorption at 525nm (%)
KOH +EG(A)	**80C/15 hrs**	**97.7/2.3**	**45**	**0.63**	**95.74/78.93**	**1.961**	**1.07**	**92.5**
KOH	80C/15hrs	98.4/1.6	1024	0.76	95.54/79.09	1.955	1.13	90.2
NaOH	120C/15hrs	98.8/1.2	1210	0.70	95.59/79.05	1.962	1.16	76.9
NaOH(B)	**80C/15 hrs**	**99.7/0.3**	**42**	**0.48**	**95.67/78.99**	**1.960**	**1.14**	**74.7**
KOH	120C/15 hrs	100/0	1125	0.36	95.71/78.96	1.961	1.11	71.9
KOH +EG	120C/15 hrs	42.5/57.5	52	0.01	95.74/78.92	1.961	1.15	68.2
NaOH +EG	120C/15 hrs	56.9/43.1	38	0.57	95.74/78.92	1.962	1.14	54.2
NH_4OH +EG(C)	**120C/15 hrs**	**99.3/0.7**	**19**	**0.10**	**95.42/79.17**	**1.952**	**1.05**	**47.4**
NaOH +EG	80C/15 hrs	95.9/4.1	31	0.04	95.40/80.03	1.938	1.12	41.0
NH_4OH(D)	**120C/15 hrs**	**99.9/0.1**	**1548**	**0.13**	**95.63/79.03**	**1.961**	**1.11**	**14.0**

On the other hand, depending on the specific point defect and its compatibility with the lattice, local vibrational modes may be introduced, which may also be Raman active.[36] The Raman spectra of Sample A shows three optical vibrational modes of CuO (279.0 cm^{-1}, 322.4 cm^{-1}, and 611.0 cm^{-1}), namely A_g, B_{1g}, and B_{2g} . The shift of these peaks towards lesser wavenumbers (red shift) and increased value of FWHM ascertains the nanostructured CuO. In addition to CuO peaks, a Cu_2O peak was also seen in Sample A at 485.2 cm^{-1} which corresponds to $2E_u$ and is assigned to multi phonon scattering, which involves vibrations of both Cu and O atoms.[36]

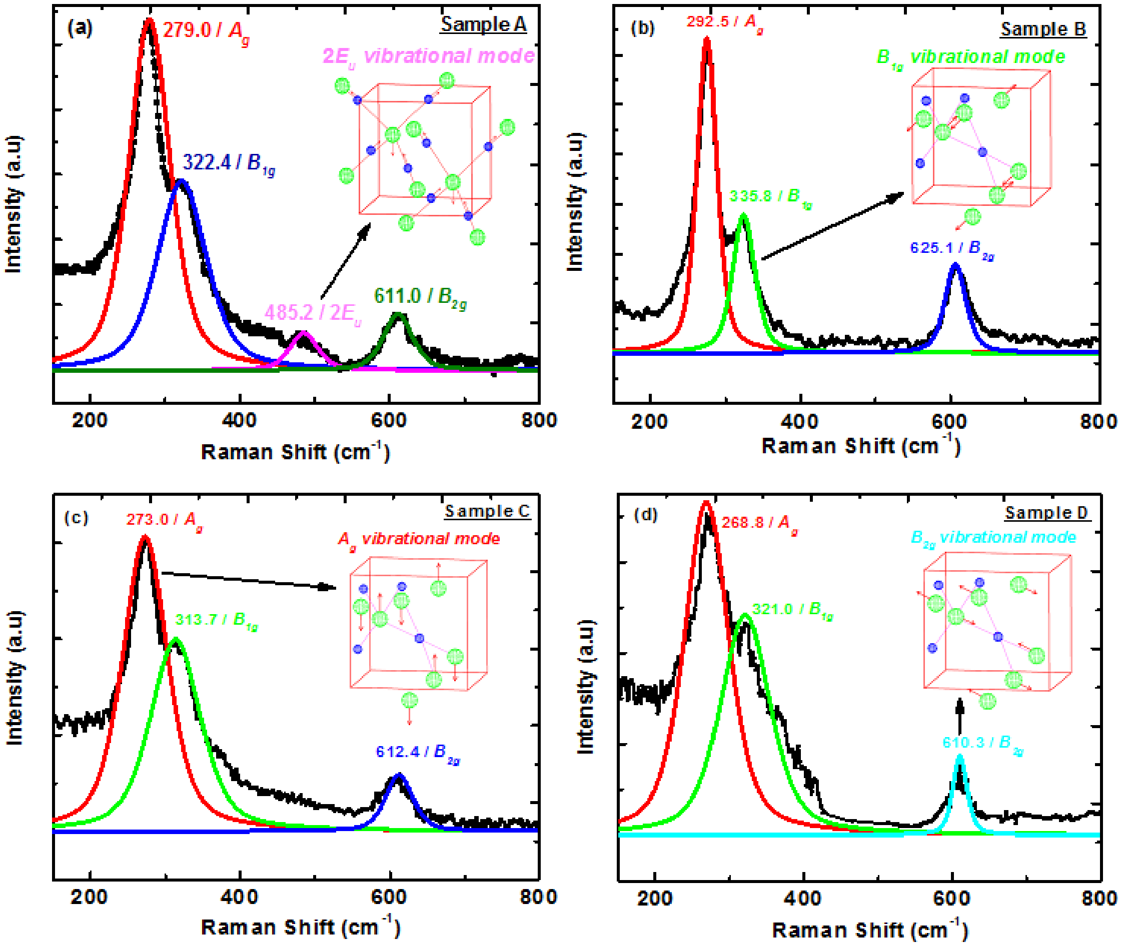

Fig. 3. Raman spectra of Sample (a) A, (b) B, (c) C, and (d) D with the Voigt peak fitted curves. The Raman active vibrational modes are also shown. The green solid spheres represents O^{2-} and the blue ones Cu^{2+}.

When the grain size increases, Raman peaks become stronger and sharper, and shift slightly to higher wavenumber (blue shift) as is seen in the case of Sample B. The frequency dependent Raman peak intensity $I(\omega)$ is a superposition of weighted Lorentzian contributions over the whole Brilloun zone is given by equation (2): [39]

$$I(\omega) = \int \frac{|C(0,k)|^2}{[\omega-\omega(k)]^2+(\Gamma o/2)^2}\, d^3k \qquad (2)$$

where, $\omega(k)$ is the phonon dispersion curve, Γo is the natural full line width and $C(0,k)$ is the Fourier coefficient of the phonon confinement function, which is often represented as equation (3):

$$|C(k)|^2 = e^{\left(-k^2d^2/16\pi^2\right)} \qquad (3)$$

where d is the average size of the nanocrystals.[41] The broadening and the red shift of a Raman peak are a result of this integration in the above mentioned equation when the grain size decreases. It should be noted that crystal defects can also result in a red shift and broadening of the Raman peak. As it is well known, nanometer-sized materials usually have many structural defects, such as oxygen vacancies in oxides, and these defects may sometimes affect the optical characteristics. The three Raman peaks in CuO arise from vibrations of the oxygen atoms only. [42] The vibrations of the oxygen ions (green) are also represented as inset figures along with the Raman spectra.[39] Studies have suggested that the changes in the spectra are mainly due to size effects and not related to oxygen deficiency.[21]

The prominent B_{2g} mode in all the samples suggests a non-polarizable nature. The giant red shift of B_{1g} to 313.7cm^{-1} indicates nanostructured morphology of sample C. In particular, this mode (B_{1g}) seems to have been affected appreciably by morphological changes in copper oxides sample. The Raman peaks for CuO shifts towards lower wavenumber in sample D suggests nanostructures and hence more defects in the resulting phase mixture. The increased values of FWHM and the red shift of the Raman peaks in sample A suggests a nanostructured phase mixture. When Cu_2O is placed in contact with a metal to form a Schottky barrier, most metals reduce Cu_2O to form a copper rich region at the interface, which dictates the barrier -height magnitude. This reduction phenomena, coupled with inter diffusion of copper results in low efficiencies, necessitating a heterojunction design, which increases the complexity of the solar cell device. Sample A shows a much more stable structure, as the Raman peaks shifts towards lower wavenumbers and thus can be an excellent material for solar cell applications.

Raman spectra are normally determined by the crystal structure of the sample and the relative orientation between its crystal axes and the polarization direction of the incident laser. However, for nano materials when the size of the sample is smaller than the focus spot size of the laser, the shape of the sample also becomes a contributing factor to the Raman spectra because the effective electric field inside the sample can be different along different directions due to polarization. Raman spectroscopy has played a unique and significant role in the study of nanostructures.[43,44,45]The angle θ between the long axis of the copper oxide nanostructures and the polarization direction of the incident laser is adjusted between 0 degrees and 180 degrees in steps of 45 degrees using a analyzer and polarizer. All the Raman active modes are stronger when the polarization direction of the incident laser is parallel to the long axis of the nanostructures ($\theta=0$ or $\theta=180$) and weakest in perpendicular geometry ($\theta=90$). Interestingly it may be noted that the strongest Raman signals are achieved at 45 degrees and 135 degrees. This may be related with the shape and size of the copper oxide nanostructures, and will be a major part of our research work in near future. The signal strength of all the Raman active modes especially B_{2g} increases at 45 degrees and drops down at 90 degrees, and increases thereafter at 135 degrees when it’s the highest and thereby returns to its initial state at 180 degrees. As observed by Chen *et al.* [46]from Raman tensors, the A_g and two B_g modes of bulk single crystal CuO have different polarization dependence.

The polarization dependence of copper oxide nanostructures can be explained using the classical electromagnetic theory. The electric field inside a one dimensional nanostructure the wavelength of laser beam could be dramatically attenuated when the incident laser is polarized perpendicular to the long axis of the nanostructures, and is represented by equation (4):

$$E_i = \frac{2€_0}{€+€_0} E_e \qquad (4)$$

where, E_i is the electric field inside the nanorods, E_e the excitation field, and $€(€_0)$ is the dielectric constant of the nanostructure (vacuum). [47] The polarization dependence of Raman modes in free-standing copper oxides nanostructures is dominated by the adjustment of the electric field inside nanorods and big dielectric contrast between these nanorods and their surroundings. The Raman polarization measurements are given in the supplementary section.

Scanning electron microscopy (SEM)

SEM images of the four selective hydrothermally synthesized copper oxide samples (A, B, C, D) are shown in Figure 4. Sample A shows a unique one dimensional lassie nanostructure measuring less than 50nm. SEM imaging of sample B shows 1D rod like nanostructured copper oxide which is considerably larger in size than the lassie nanostructure present in sample A, which is likely due to the lower pH of the base used. An increased reaction temperature facilitates conglomeration of the rods into flower shaped nanostructures. Sample C shows nano fibril structure of copper oxides measuring less than 30nm. In sample D, stacked copper oxide rods can be seen, which attains the morphology of a flower. The pH of the base used is considerably lower, which can be the reason for lesser number of XRD peaks for copper oxide in the sample. Uniqueness of the nanostructured morphology can play a crucial role in optical absorption properties. In particular, the entanglement of the 1D nano-lassie structure in sample A can increase the solar absorption properties by trapping light. The enhanced solar absorption is likely due to the unique 1D nanostructure, as well as to the phase percentages of the copper oxide formed. Introduction of EG serves the purpose of reduction above certain temperatures, where unique morphologies of copper oxides are formed.

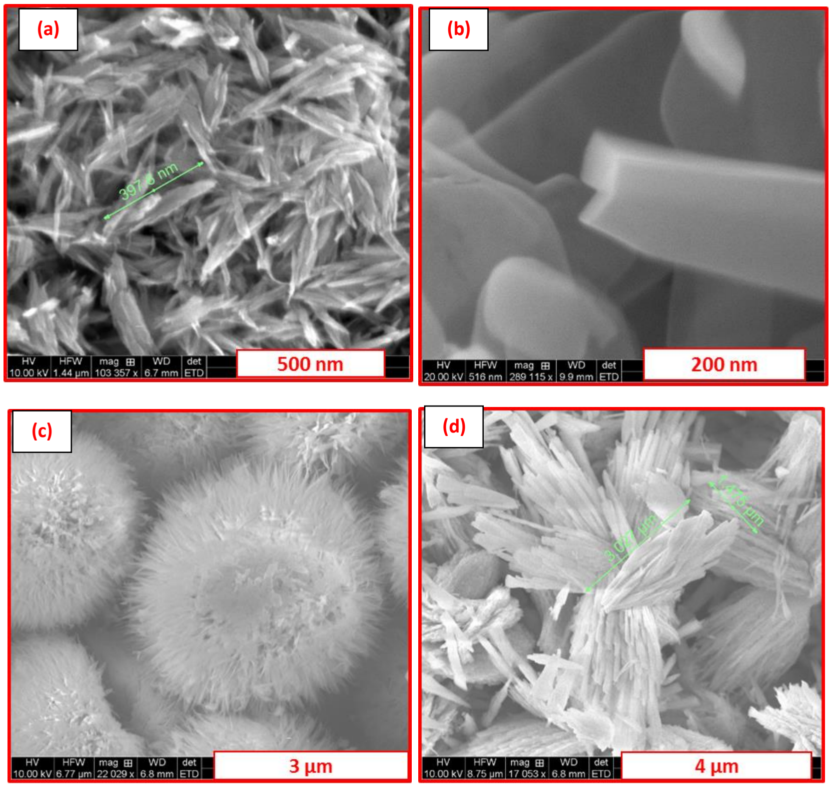

Fig. 4. SEM images of Samples (a) A, (b) B, (c) C, and (d) D. The solar absorption characteristics are also dependent on the morphology of the copper oxides synthesized.

So, it can be seen that varied morphology of copper oxide can be synthesized by a hydrothermal process, which opens the road map for engineering improved forms of copper oxides for various optoelectronic devices.

Optical absorption

The optical absorption of an electromagnetic wave by a quantum system is responsible for decay of intensity of the wave with an absorption coefficient (∝) of the material, and is represented in the equation (5):

$$I(x) = Io\, e^{(-\propto x)} \qquad (5)$$

The energy loss by the wave per unit volume is given by equation (6):

$$\left({}^{P}/_{v}\right) = I \qquad (6)$$

This energy loss favors electronic transitions which forms the basis of solar cells. So, an increase in absorption coefficient is highly desirable for better efficiency of a solar cell. The stacked solar transmitted intensity of all hydrothermally synthesized samples is shown in the Figure 5.

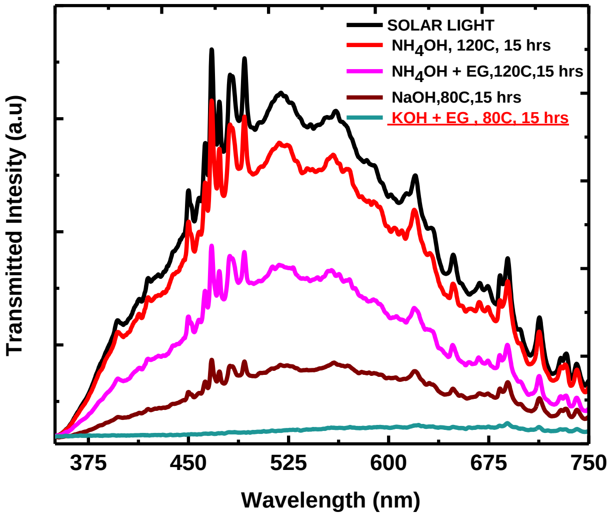

Fig. 5. Variation of solar transmitted intensity of hydrothermally synthesized copper oxide samples with wavelength of the solar lamp used. The stacked plots indicate that samples are having varied optical band gap, and thus possess different optical absorption characteristics. The red underlined sample (A) has the highest optical absorption coefficient.

This is a direct consequence of the change in absorption coefficient which is due to change in energy band gap, and unique morphology of the samples. It is quite obvious from the above plots that sample A exhibits the largest optical absorption properties in the visible solar spectrum.

To further understand this unusual behavior extensive analysis of the optical data has been carried out. The band gap of sample A was calculated using the Tauc's formula and is shown in Figure 6. The optical direct and indirect band gap of CuO nanoparticles was extracted according to the following equation (7): [48,49]

$$\propto = \frac{B(hv - Eg)^{n}}{hv} \qquad (7)$$

where, hv is the incident photon energy, ∝ is the absorption coefficient, B is a material dependent constant and Eg is the optical band gap.

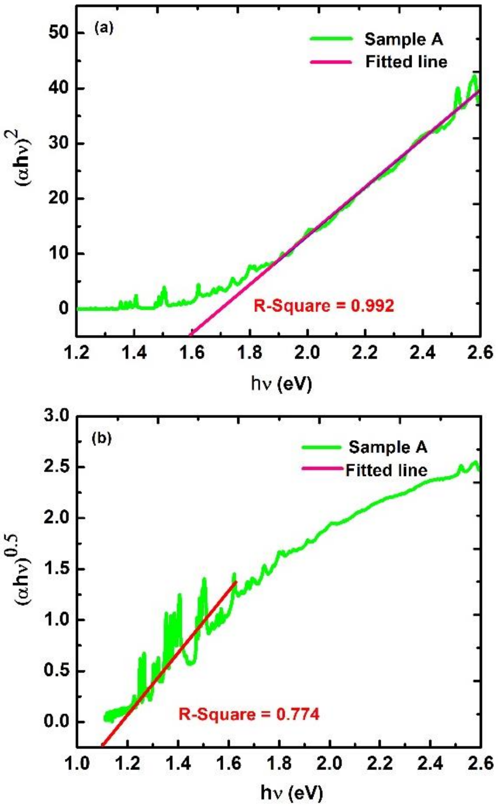

Fig. 6. Tauc plot for calculating (a) direct and (b) indirect band gap of sample A. The sample A has a direct band gap of 1.60eV and an indirect band gap of 1.10eV.The higher degree of linearity in the direct band gap calculations predicts the predominance of direct band gap in sample A.

The value of *n* depends on the nature of transition. To calculate the indirect band gap transition $(\propto h\nu)^{0.5}$ is plotted against photon energy (hν). The intercept of the straight line on the hν axis corresponds to the optical band gap (E_g). The calculated direct and indirect band gap for sample A using Tauc's plot is 1.60eV and 1.10eV respectively. The resulting direct band gap approaches the Shockley-Queisser limit for maximum solar cell efficiency (1.34eV).[50] Studies have shown that incorporation of intermediate band gap energies can actually increase solar cell efficiencies.[51] The shift in the direct band edges as seen in the present case is due to the quantum confinement effect,[52,53] which is evident from the energy band calculations of sample D. The calculated energy gap in sample D (1.1 eV) may be due to absorption involving defect states.

The reported value of direct energy band gap for pure CuO is 1.2eV,[54] which is the same as that calculated in Sample D. The absorption coefficient is calculated by the following equation (8):

$$\propto = \frac{1}{t}\left(\frac{1}{\ln(T)}\right) \qquad (8)$$

where, t is the thickness and T is the transmittance. We calculated the value of $\propto_1 t$ and $\propto_2 t$ for sample A and D, where $\propto_1$ and $\propto_2$ are the absorption coefficients of samples A and D. Sample D corresponds to pure CuO as determined by the phase percentage calculated by Rietveld analysis, and the direct energy band gap calculations.

To better understand the excellent optical absorption properties of sample A, we also investigated the optical properties of physical mixtures prepared from commercially available micro particles of CuO (Alfa Aesar-99.7% metal basis) and Cu_2O (Alfa Aesar-99.9% metal basis) in the same phase percentages as sample A. The solar transmitted intensity plot shown in the Figure 7 shows that sample A absorbs higher amount of solar light than the physical mixture. It should also be noted from Figure 7 that the absorption coefficient of sample D is about the same as that of commercially available pure CuO (Alfa Aesar-99.7% metal basis). It is important to compare the optical absorption properties of sample A with currently utilized solar cell materials. The variation of absorption coefficient ∝ of sample A along with pure CuO and widely used solar cell material Si as a function of wavelength is shown in Figure 8. It can be clearly seen from the Figure 8 that ∝ tends to decrease exponentially as the wavelength increases. This behavior is typical for many semiconductors and can occur due to internal electric fields within the crystal, deformation of lattice due to strain caused by imperfection, and inelastic scattering of charge carriers by phonons.[55]

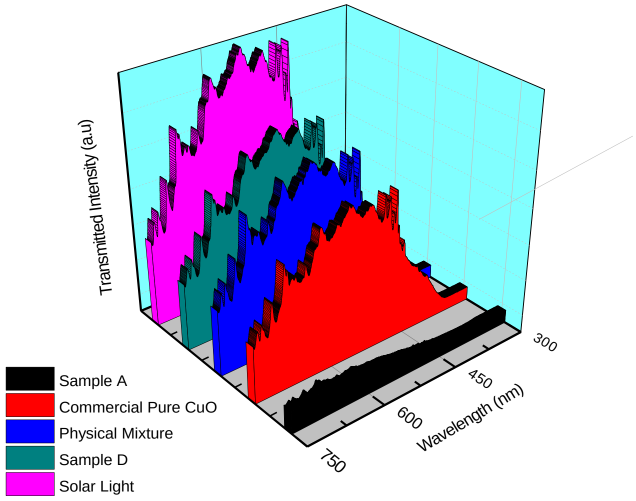

Fig. 7. Demonstration of superior solar transmitted intensity of Sample A. The sample absorbs more light than commercially available pure CuO, physical mixture of copper oxides and sample D.

The most interesting result is that the optical absorption coefficient of sample A is significantly larger as compared to pure CuO and is nearly double when compared with a conventionally used solar material, Si. This increase in ∝ of sample A is attributed to the nano particulate size, direct band gap, phase percentage, and lassie morphology of the copper oxide. Increased value of α will decrease the thickness of the copper oxide solar cell thereby decreasing the material usage in the fabrication process. Studies have confirmed that the optical absorption spectra and polarization properties in an extensive series of quasi-two dimensional copper oxides, including the simplest oxide CuO, shows that the fundamental absorption band at 1.0-1.5 eV (in different oxides) is associated with an allowed b_{lg} - e_u transition (e_u, is the hybrid e_u (π) - e_u (σ) state).[56]

The figure 8 represents variation of optical absorption coefficient with wavelength of sample A compared to commercial pure CuO[57] and Si[58]. The Sample A possess significantly large optical absorption coefficient in the visible range as compared to Si and commercial pure CuO.

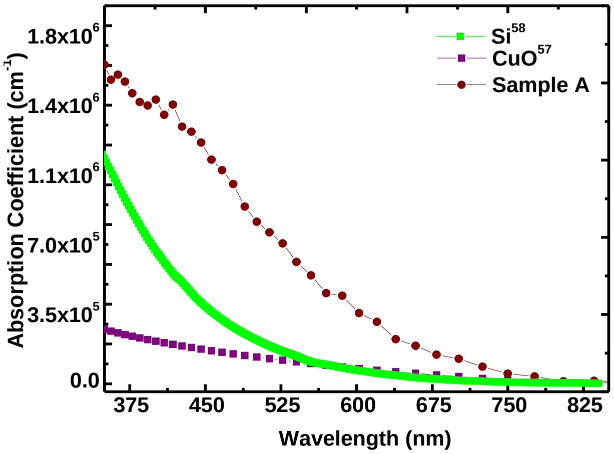

Fig. 8. Variation of optical absorption coefficient with wavelength of sample A compared to commercial pure CuO and Si. The Sample A possess significantly large optical absorption coefficient in the visible range as compared to Si and commercial pure CuO.

The increase in absorption coefficient also increases the extinction coefficient (k), which is defined as the imaginary part of the complex refractive index and represented in equation (9):

$$k = \frac{\propto\lambda}{4\pi t} \qquad (9)$$

Increased values of extinction coefficients are favored for designing anti-reflective coatings on solar cells. Thus, it can be proved that hydrothermal synthesis can be employed to synthesize varied energy band gap copper oxides nanoparticles. By introducing a buffer layer of varying energy gap in between copper oxide solar cells, fewer recombination sites should be available for the excited carriers. With these methods for improving efficiencies, copper oxide is a potentially attractive material for photovoltaic cells. In a general case, the carrier generation as a proportion of incoming photons of a given energy can be written as equation (10):[59, 60, 61]

$$g(E,x) = \big(1 - R(E)\big) \propto (E) b(E) e^{-\int_0^x \propto(E,x)dx} \qquad (10)$$

Where, b(E) is the incident photon flux and R(E) is the reflectivity to normally incident light of energy E. In order to obtain the total rate of generation of charge carriers ($G(x)$) it is necessary to integrate over the range of photon energies that could result in a charge carrier being generated is represented in equation (11): [54, 55, 56]

$$G(x) = \int g(E,x)dE \qquad (11)$$

When the incoming energy of a photon is greater than the band gap charge carriers with an increased amount of kinetic energy are created, however this energy is soon lost due to collisions in the crystal lattice until the energy is reduced to E_g; this process is known as thermalization. An increase in the range of photons absorbed by the synthesized copper oxide nanoparticles can help for better fabrication of solar cell devices. The photo current density (J) produced in an external circuit can be formulated as shown in equation (12): [52, 53, 54]

$$J = q \int_E^{E+dE} b(E) QE(E) dE \qquad (12)$$

Where, b(E) is the incident spectral photon flux density i.e. the number of photons in the range E to (E + dE) that fall upon the unit area of the photovoltaic surface per unit time. Quantum efficiency (QE) and hence the current density is dependent upon the absorption coefficient of the solar cell material. Deviations in the reported values may arise due to different models that have been used to extract the optical properties from measured quantities. This not only affects the value of the band gap but also affects the interpretation of the nature of the gap (i.e. direct or indirect).

Photoluminescence (PL) spectroscopy

The room temperature PL spectra using the laser excitation source of 325nm, of sample A along with the peak fitted Gaussian and Lorentzian curve using Labspec software is shown in Figure 9. Emission peaks are observed at 2.9eV (427nm-violet), 2.3eV (540nm-green), 2.1eV (590nm-yellow), 1.8eV (690nm-red), 1.6eV (775nm-near IR), 1.5eV (827nm- near IR), 1.3eV (954nm- near IR), and 1.2eV (1033nm- near IR). The emission at 427nm corresponds to band-edge emission.[62] The second one at 2.3eV arises from the singly ionized oxygen vacancy resulting in green emission of CuO materials because of recombination of a photo generated hole with a singly ionized electron in valence band.[63] The fluorescence at all other points arises due to band to band transition of copper-oxide and other defects arising in the nanostructured mixture. The luminescence peak corresponding to 2.3 eV is also due to band to band transition of CuO. A transition from conduction band to acceptor level (above the valence band) takes place and correspond to an emission at 2.1 eV , while another transition from donor level (below the conduction band) to valence band and acceptor level with emitting fluorescence of energy 2.1eV. Out of these transitions, a transition from electron trapping level (below the conduction band) to valence band take place with a fluorescence of energy 2.1 eV through a non-radiative transition from conduction band to electron trap level. Balamurugan *et al*[64] have reported defect level is due to copper ion vacancies in copper oxide. Jung *et al*[65] had also reported the PL spectrum at ~ 2.3 eV from Cu_2O NPs embedded in a polyimide layer, due to inter band transitions from the ground electronic sublevel to the ground heavy-hole sublevel of the Cu_2O NPs.

The lack of luminescence data for copper oxide can be due to its low emission efficiency. Copper oxide band gap, and in general its optical properties, have been studied by optical absorption with a dispersion of results as the reported values of 1.85 eV in thin films [66], 2.03 eV [67] and 1.2 eV [68] in nanowires, or 2.43 eV in nanoparticles[69]. Lin *et al.* [70] estimated from photoluminescence measurements a band gap of 1.67 eV in nanofibers. We predict that the 1.3 eV band, whose energy is close to the band gap value reported in several absorption measurements, corresponds to near band edge transitions of CuO. The bands peaked at lower energies may correspond to defect levels. Previous spectrally resolved photocurrent measurements [71] actually revealed the existence of recombination centers lying 1.2 eV below the conduction band edge in CuO samples with a band gap of 1.3 eV. Furthermore, recent theoretical calculations indicate that although Cu vacancies are the most stable defects in CuO, they do not introduce new states within the band gap [72]. Hence, Cu vacancies might not be involved in the mentioned emissions. On the contrary, calculations reveal that such states can be introduced by oxygen vacancies and antisite defects[73]. The formation energy of O_{Cu} antisite defects of acceptor nature is actually only slightly higher than the formation energy of Cu vacancies[12]. In any case, it is currently recognized [74] that a systematic study of the stoichiometry and defect structure of CuO, particularly in samples grown in a wide range of well-defined equilibrium conditions, is still necessary.

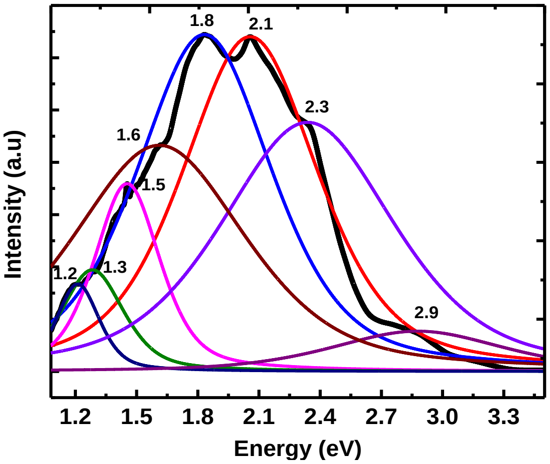

Fig. 9. Photoluminescence spectra of Sample A. The electronic transitions are observed in the visible to near IR region, which proves that the mixture can absorb a wide range of solar energy. This proves that the hydrothermally prepared nano mixture can be used as an excellent material for solar cell applications.

The photoluminescence spectrum of nanoparticles shows a broad luminescence in the visible region which indicates that these nanoparticles can be applicable for fabrication of photonic devices. The electronic transitions as seen from the PL spectra, at 590nm and 690nm are the greatest, which corresponds to the peak of the solar absorption spectra. Some electronic transitions are also observed in the near IR region, which proves that the mixture can absorb a wide range of solar energy. The PL spectra proves that the hydrothermally prepared mixture can be used as an excellent material for solar cell applications.

Mechanism of formation

Studies from the previous researchers revealed that, under supercritical conditions, the following three-step mechanism is involved in the formation of oxide nanoparticles from the metal salts:[75]

(1) The ion product of water (K_w) considerably increases, giving rise to higher concentrations of OH^- ions and more rapid hydrolysis of the metal cations (reactions 13 and 14).

(2) The dielectric constant of water declines and, accordingly, its solvent power for dissolving ionic materials also reduces. Reducing the solvent power of water elevates the tendency of the hydroxide molecules (reaction 15) for immediate precipitation, which, in turn, leads to the creation of a larger number of the precipitate nuclei and, thus, the formation of the nanosized particles.

(3) Because of the high-temperature conditions, unstable transition-metal hydroxides are converted to their corresponding oxides (reaction 15).

Water dissociation: $H_2O \longrightarrow H^+ + OH^-$ (13)

Hydrolysis: $Cu^{2+} + 2OH^- \longrightarrow Cu(OH)_2$ (14)

Dehydration: $Cu(OH)_2 \longrightarrow CuO + H_2O$ (15)

The morphology of CuO nanostructures without introduction of EG into the hydrothermal process is determined by the crystallographic structure of $Cu(OH)_2$ precursor.[76] At room temperature, orthorhombic $Cu(OH)_2$ first precipitates in the solution. The (010) plane in orthorhombic $Cu(OH)_2$ structure is a corrugated sheet structure. By the phenomenon of edge sharing, a sheet of distorted $Cu(OH)_6$ octahedral is formed. The 2D layers of these sheets parallel to the (010) plane are connected through H-bonds. When the reaction temperature and time increases to a certain extent, due to the action of the excess OH^-, the orthorhombic $Cu(OH)_2$ transforms to monoclinic CuO nanostructure by a dehydration reaction breaking the interplanar H-bonds.[77] It's also known that the crystal growth habit is not only determined by internal structure but is also affected by external conditions. When a certain quantity of EG is introduced into the hydrothermal process, it is believed that under a certain range of alkaline conditions the hydrogen bonds of EG can attack the OH-bonds protruding out of the edge of orthorhombic $Cu(OH)_2$. Consequently, the orthorhombic $Cu(OH)_2$ was activated and the dehydrated reaction took place more easily at the positions attacked by EG. In this way and with the lapse of time at higher reaction temperatures, the nuclei of monoclinic CuO are formed by the dehydration of the orthorhombic $Cu(OH)_2$.[40] Figure 10 represents a schematic of the nanostructured copper oxides formed by the action of the base and EG. The connecting hydrogen bonds between (010) crystallographic planes of $Cu(OH)_2$ are being acted upon by the OH^- of the base. The OH bonds in $Cu(OH)_2$ are being activated by H atom in EG. Dehydration reaction results in the flower like morphology of copper oxides. The green atoms represents O, red ones Cu atoms and yellow ones are H atoms. The formation of lassie nanomorphology depends on the reaction parameters, base and EG used during hydrothermal synthesis. Therefore, EG plays a critical role in the formation of monoclinic nanostructured copper oxides. However, EG also acts as a reducing agent above certain reaction temperatures. As a result, a small quantity of cubic Cu_2O with the flower-like morphology coexists with CuO nanostructures. Because of the internal symmetry crystallographic structure of cubic Cu_2O, it can grow along the 3D directions around it. Therefore, at the positions modified by EG, the nuclei of Cu_2O grow bigger and longer along the radial directions.[78] Higher pH of the base used in hydrothermal synthesis and reaction temperatures and time favors formation of CuO, which have distinctly different solar absorption properties. Introduction of EG in the system reduces some CuO to Cu_2O, which also alters the morphology, size and optical absorptions characteristics which is schematically shown in Figure 10. The uniqueness of this study deals with the correlation of the significantly large optical absorption coefficient of nanostructured copper oxides with the structural conformity, optical-phonon vibrational modes, morphology, optical band gap calculations, and photoluminescence spectra. Sample A was observed to have the largest optical absorption characteristics, which was significantly more than commercially available CuO and nearly twice that of Si, was a particular phase mixture of copper oxides. The Rietveld analysis confirmed the phase mixture to be 97.7:2.3 ($CuO:Cu_2O$). The sample has a minimal perturbation of the bond angles and bond lengths, as calculated by Rietveld analysis. This can reduce the localized tail states, which acts as effective recombination sites. The mobility of the charge carriers are the least in these states, and reduction of these states can thereby enhance solar cell efficiency. Stable inorganic oxide nanostructures are highly desirable for better working heterojunction solar cell devices.

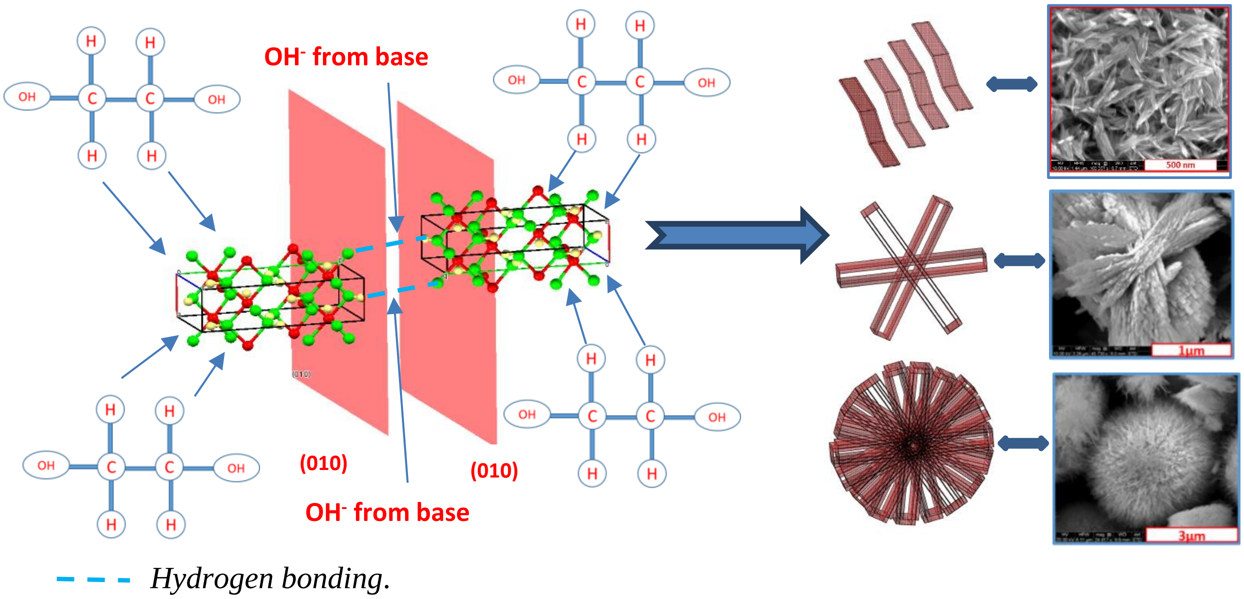

Fig. 10. Schematic representing the mechanism of formation of 1D nanostructured copper oxides. Nanostructured copper oxides of varied morphology are formed by changing the base media and introduction of EG during the hydrothermal growth.

Studies have also shown that incorporation of intermediate band gap energies can actually increase solar cell efficiencies. The electronic transitions studies as seen from the PL spectra, at 590nm and 690nm are the greatest, which corresponds to the peak of the solar absorption spectra. Some electronic transitions are also observed in the near IR region, which proves that the mixture can absorb a wide range of solar spectrum.

Experimental

Synthesis of copper oxide composite nanoparticles

All the chemicals were analytic grade reagents and used without further purification. The experimental details were as follows; (0.15M) $CuSO_4\cdot 5H_2O$ (GFS Chemicals-Assay 98.0-102.0%) was dissolved in (20 ml) deionized HPLC water (GFS Chemicals- Resistivity at 25 C is 18.0 Mohm-cm) under stirring. (45% (W/W)) of KOH (GFS Chemicals- Assay 45%) was added to the resulting aqueous solution till the pH of the solution was 13. Then, the solution was transferred into Teflon lined stainless steel autoclaves, sealed and maintained at different reaction temperatures (80 C and 120 C) for 15 hours. In order to investigate the growth mechanism and the action of Ethylene glycol (EG), the experiments were carried out with the addition of (10ml) EG (GFS chemicals-99% pure) to the aqueous solution at the same reaction parameters mentioned above. After the completion of the hydrothermal process, the solid products were centrifuged (LW Scientific centrifuge-Model E8) at a rotation speed of 30 revolutions s^{-1} for 30 min, washed three times with distilled water and ethyl alcohol (Fisher Scientific, anhydrous and denatured) respectively to remove the ions possibly remaining in the final product, and finally dried at 100 C in air. Powder samples were also prepared using (50% (V/V)) NaOH (GFS chemicals- Assay 48-52%), and (10% (V/V)) NH_4OH (GFS chemicals- Concentration 10.0 +/- 0.5%), which possess different basicity as compared to KOH.

Powder X-ray diffraction studies and Rietveld analysis

The obtained samples were characterized using X-ray powder diffraction (Bruker, D8 Discover) θ–2θ scan with CuK_{α} (λ=1.5405Å). Rietveld analysis was done using Diffrac ^{plus} Topas software. Special care was taken for a quality data collection, background contribution, peak- shape function, refinement of the profile parameters as well as the structure parameters and interpretation of the agreement indices (R values), in the due course of the XRD analysis. The Bragg Brentano reflection geometry was employed for collection of the crystallographic pattern. Factors that were considered prior to the collection of the XRD data were the geometry of the X ray diffractometer, alignment, proper calibrations, thickness of the sample, slit sizes, and adequate counting time. For Bragg Brentano geometries, it is important that the incident beam be kept on the sample at all angles to ensure a constant volume condition. Quite often, the divergence slits used are too wide and the beam hits the sample holder at low angles, so the intensities measured at these angles are too low.[79] Henceforth, we used 0.6mm for both primary and secondary divergence slit. To ensure good counting statistics throughout an X ray powder diffraction pattern, more time should be spent on data collection at high angles where the intensities are lower. We employed counting time of 6 seconds for a good quality XRD pattern. The assumption for refection geometry is that the sample is infinitely thick and thus a considerable time was spent on proper sample preparations. Preferential orientations were calculated with the help of March Dollase function. The goodness of fit (GOF) appreciably approached 1 with the incorporation of sophisticated corrections using spherical harmonics. Any temptation to smooth the diffraction data before doing a Rietveld refinement was resisted. Smoothing introduces point-to-point correlations (off diagonal weight matrix elements) which results in aberrant refinement values. The emission profile was considered for all the values of Cu K alpha radiations. Chebychev background correction was done of the order of 5. The Goniometer primary and secondary radii were carefully incorporated in the program with the consideration of the primary and the secondary soller slits used. The zero error and the absorption were refined in the process for better results. The Lorentz Polarization factor was fixed throughout the analysis. The peak profile function used for the refinement is Fundamental parameter (FP). These numerical convolutions have a high degree of accuracy as they comprise analytical Lorentzian and Gaussian functions convoluted with straight line segments. The fundamental parameters approach (FPA) provides a complete description of the geometric instrument response. All parameters in FPA models are physically based, with parameters that map directly onto the geometry of the diffractometer. This facilitates the interpretation and evaluation of the line profile model fit.[80] The Debye Waller temperature factor was fixed throughout the refinement process. The refinement was carried out carefully to minimize the errors due to increase in the number of variable parameters. The lattice parameter was calculated from the Pawley fitting (unrestrained fitting of parameters) which was fixed in the preceding Rietveld refinements. The space coordinates, and the temperature factors for the ions were not refined in the Rietveld analysis.

Raman micro-scattering spectroscopic analysis and photoluminescence measurements

The vibrational phonon modes were determined by Raman spectroscopy using 532nm green laser (Horiba Labram Raman-PL). Photoluminescence measurements were carried out employing 325nm UV laser using the abovementioned instrument. The Raman spectra and PL spectra was analyzed using Gaussian and Lorentzian peak fittings in NSG Lab spec software.

Optical absorption measurements

0.4mg of the hydrothermally synthesized powder was dissolved in 3ml double deionized water and the resulting solution was transferred to cuvettes for further optical characterization. Absorption characteristics spectra were measured by Ocean Optics HR 4000 spectrometer in conjunction with Ocean Optics Spectra suite software. The solar light (Newport 69907 light source) was used for solar cell simulation. We were extremely cautious during the absorption measurements. Many transmission spectra were taken repeatedly in small intervals to make sure that there were no errors during the measurement. Collection of the absorption spectra takes less than 5 seconds as we used the Ocean Optics software which takes spectral readings on instantaneous basis. We have taken several measurements to assure the integrity of the presented data. We have also seen that the powder remains in the solution for a considerable period of time before it settles down.

For calculating “t” we have employed a trivial but unique method. First, we collected the transmission spectra for commercially pure copper oxide (with known optically absorption coefficient). It must be noted that same amount of powders were mixed with the same volume of DI water for making the solutions which were being used for optical absorption calculations. We used equation (8) for calculating of (α_{CuO}*t) from the transmittance spectra. It should be noted that since transmittance varies with the wavelength of source light, so the value of (α_{CuO}*t), will also vary with the wavelength of source light. Then, we collected the transmittance spectra of synthesized nanostructured copper oxide samples. This gives us the value of ($\alpha_{sample\ A}$*t). Then we take the ratio of these two values i.e (α_{CuO}*t) : ($\alpha_{sampleA}$*t). α_{CuO} is known from standard calculations, and thus we can find out $\alpha_{sampleA}$. Again, $\alpha_{sampleA}$ is a function of wavelength of light, and we took the value at the peak of visible solar spectrum (i.e at 525nm) and compared the same with that of standard Si at that point. To prove the correctness of the procedure used we synthesized nanopowder copper oxide with the same band gap as that of commercially available CuO. We measured transmittance spectra of the synthesized powder and it is in accordance to that of commercially available CuO.

Scanning electron microscopy

The morphology of as-prepared samples were characterized by scanning electron microscopy (FEI Quanta 200S). Carbon adhesive tapes were being employed during EDX measurements.

Conclusions

Nanostructures of copper oxides with high optical absorption coefficient have been synthesized by energy efficient hydrothermal process. The solar absorption coefficient of the hydrothermally prepared nanostructured phase mixture of copper oxide is significantly large as compared to commercially available pure CuO and is nearly double when compared with Si. This significant increase in solar optical absorption can be attributed to the lassie nanostructure, change in energy band gap and a particular phase mixture of copper oxides. Investigation of the growth mechanism indicates that EG plays a critical role in the formation of mixture of copper oxides, and modifies the morphology of the nanostructures. The ability to engineer nanostructured phase mixture of copper oxides with large optical absorption coefficient can lead to resurgence of CuO based solar cells. The formation mechanism discussed in this paper opens a new approach in synthesis of similar morphological nanostructures for highly efficient solar cell applications.

Acknowledgments

This research was funded by National Science Foundation, Grant Numbers: DMR-1126375, and DMR-0907037, Missouri State University, and CASE exploratory research funding. The authors would like to acknowledge A. Haque, M. N.

Taufique, R. Rahaman and P. Karnati for proof reading this research article.

References

1 Y. Abdu and A. Musa, *Bajopas.*, 2009, **2**, 8.
2 S. Agarkar, V. Dhas, S. Muduli and S. Ogale, *RSC Advances*, 2012, **2**, 11645.
3 A. Frank, N. Kopidakis and J. van de Lagemaat, *Coord. Chem. Rev.*, 2004, **248**, 1165.
4 M. Law, L. Greene, J. Johnson, R. Saykally and Y. Peidong, *Nature Materials*, 2005, **4**, 455.
5 T. Oekermann, D. Zhang, T. Yoshida and H. Minoura, *J. Phys. Chem. B*, 2004, **108**, 2227.
6 N. Lewis, *Science*, 2007, **315**, 798.
7 W. Huynh, J. Dittmer and A. Alivisatos, *Science*, 2002, **295**, 2425.
8 O. Bisi, S. Ossicini and L. Pavesi, *Surf. Sci. Rep*., 2000, **38**, 1.
9 L. Pavesi, L. Dal Negro, C. Mazzoleni, G. Franzo and F. Priolo, *Nature*, 2000, **408**, 440.
10 J. Zhang, H. Liu, Z. Wang, N. Ming, Z. Li and A. Biris, *Adv. Funct. Mater*., 2007, **17**, 3897.
11 W. Yuxin, L. Xinyong, W. Ning, Q. Xie and C. Yongying, *Sep. Purif. Technol.*, 2008, **62**, 727.
12 N. Kopidakis, K. Benkstein, J. van de Lagemaat, A. Frank, Q. Yuan and E. Schiff, *Phys. Rev. B: Condens. Matter Mater. Phys.*, 2006, **73**, 7.
13 K. Zhu, N. Neale, A. Miedaner and A. Frank, *Nano Lett*., 2007, **7**, 69.
14 R. Asahi, T. Morikawa, T. Ohwaki, K. Aoki and Y. Taga, *Science*, 2001, **293**, 269.
15 B. Faughnan and R. Crandall, *Appl. Phys. Lett*., 1977, **31**, 834.
16 R. Jin, Y. Cao, E. Hao, G. Metraux, G. Schatz and C. Mirkin, *Nature*, 2003, **425**, 487.
17 Y. Xia, P. Yang, Y. Sun, Y. Wu, B. Mayers, B. Gates, Y. Yin, F. Kim and H. Yan, *Adv. Mater.*, 2003, **15**, 353.
18 M. Grätzel, *Nature*, 2003, **421**, 586.
19 D. Wu and W. Zhang, *Phys. Rev. B: Condens. Matter Mater. Phys.*, 2006, **73**, 235206.
20 A. Mittiga, E. Salza, F. Sarta, M. Tucci and R. Vasanthi, *Appl. Phys. Lett*., 2006, **88**, 163502.
21 H. Kidowaki, T. Oku, T. Akiyama, A. Suzuki, B. Jeyadevan and J. Cuya, *J. mater. sci. res.*, 2012, **1**, 138.
22 M. Zeman and J. Krc, *Mater. Res. Soc. Symp. Proc.*, 2007, **989**, A03-01.
23 S. Kugler, *J. Phys.: Conf. Ser*., 2010, **253**, 1.
24 K. Nomura, H. Ohta, A. Takagi, T. Kamiya, M. Hirano and H. Hosono, *Nature*, 2004, **432**, 488.
25 S. Asbrink and L. Norrby, *Acta Crystallogr. B.*, 1970, **26**, 8.
26 R. Street, *Philos. Mag. Part B.*, 1984, **49**, L-15.
27 J. Chrzanowski and J. Irwin, *Solid State Commun*., 2009, **70**, 11.
28 H. Goldstein, D. Kim, P. Yu, L. Bourne, J. Chaminade and L. Nganga, *Phys. Rev. B: Condens. Matter Mater. Phys.*, 2009, **41**, 7192.
29 J. Nye, *Physical Properties of Crystals: Their Representation by Tensors and Matrices*, Oxford University Press, London 1957.
30 R. Loudon, *Advan. Phys*,. 1964, **13**, 423.
31 H. Hagemann, H. Bill, W. Sadowski, E. Walker and M. Francois, *Solid State Commun*., 1990, **73**, 447.
32 M. Balkanski, M. Nusimovici and J. Reydellet, *Solid State Commun*., 1969, **7**, 81.
33 C. Carabatos and B. Prevot, *Phys. Status Solidi B.*, 1971, **44**, 701.
34 K. Huang and *Z. Physik*, 1963, **171**, 213.
35 E. Kroumova, M. Aroyo, J. Perez-Mato, A. Kirov, C. Capillas, S. Ivantchev and H. Wondratschek, *Phase Transit*., 2003, **76**, 155.
36 B. K. Meyer, A. Polity, D. Reppin, M. Becker, P. Hering, P. Klar, T. Sander, C. Reindl, J. Benz, M. Eickhoff, C. Heiliger, M. Heinemann, J. Blasing, A. Krost, S. Shokovets, C. Muller and C. Ronning, *Phys. Status Solidi B.*, 2012, **249**, 1487.
37 J. Reydellet, M. Balkanski and D. Trivich, *Phys. Status Solidi B.*, 1972, **52**, 175.
38 A. Compaan and H. Cummins, *Phys. Rev. B: Condens. Matter Mater*., 1972, **6**, 4753.
39 P. Williams and S. Porto, *Phys. Rev. B: Condens. Matter Mater.*, 1973, **8**, 1782.
40 A. Compaan, *Solid State Commun*., 1975, **16**, 293.

41 J. Xu, W. Ji, Z. Shen, W. Li, S. Tang, X. Ye, D. Jia and X. Xin, *J. Raman Spectrosc*., 1999, **30**, 413.
42 J. Irwin and T. Wei, *J. Phys.: Condens. Matter.*, 1991, **3**, 299.
43 A.M. Rao, P.C. Eklund, S. Bandow, A. Thess, and R.E. Smalley, *Nature*, 1997, **388,** 257.
44 J. Chen, M.A. Hamon, H. Hu, Y.S. Chen, A.M. Rao, P.C. Eklund, and R.C. Haddon, *Science*, 1998, **282,** 95.
45 A.M. Rao, E. Richter, S. Bandow, B. Chase, P.C. Eklund, K.A. Williams, S. Fang, K.R. Subbaswamy, M. Menon, A. Thess, R.E. Smalley, G. Dresselhaus, and M.S. Dresselhaus, *Science*, 1997, **275,** 187.
46 X.K. Chen, J.C. Irwin, and J.P. Franck, *Phys. Rev. B*, 1995, **52,** R13130.
47 L.D. Landu, E.M. Lifshitz, and L.P. Pitaevskii, *Electrodynamics of Continuous Media*, Pergamon, Oxford, 1984.
48 N. Mott and E. Davis, *Electronic Processes in Non-Crystalline Materials*, Oxford University Press, New York **1971**.
49 G. Yue, D. Peng, P. Yan, L. Wang, W. Wang and X. Luo, *J. Alloys Comps.*, 2009, **468**, 254.
50 W. Shockley and H. Queisser, *J. Appl. Phys.*, 1961, **32**, 510.
51 A. Luque and A. Marti, *Phys. Rev. Lett.*, 1997, **78**, 514.
52 S. Neeleshwar, C. Chen, C. Tsai, Y. Chen, C. Chen, S. Shyu and M. Seehra, *Phys. Rev. B: Condens. Matter Mater*., 2005, **71**, 201307.
53 P. Mallick and S. Sahu, *Nanosci. Nanotechnol*., 2012, **2**, 71.
54 B. Balamurugan and B. Mehta, *Thin Solid Films*, 2001, **396**, 90.
55 A. Sawaby, M. Selim, S. Marzouk, M. Mostafa and A. Hosny, *Phys. B*, 2010, **405**, 3412.
56 M. Kelly, P. Barboux, J. Tarascon and D. Aspnes, *Phys. Rev. B: Condens. Matter Mater.*, 1989, **40**, 6797.
57 T. Maruyama, *Sol. Energy Mater. Sol. Cells*, 1998, **56**, 85.
58 M. Green, *Sol. Energy Mater. Sol. Cells*, 2008, **92**, 1305.
59 P. Würfel, *Physics of Solar Cells: From Principles to New Concepts*, Wiley-VCH, Weinheim, Germany 2005.
60 D. Neaman, *Semiconductor Physics and devices: Basic Principles*, McGraw-Hill, Boston 2003.
61 M. Green, *Solar Cells; Operating Principles, Technology and System Applications*, Prentice-Hall 1982.
62 R. Ningthoujam, N. Gajbhiye, A. Ahmed, S. Umre and S. Sharma, *J. Nanosci. Nanotechnol*., 2008, **8**, 3059.
63 K. Vanheusden, W. Warren, C. Seager, D. Tallant, J. Voigt and B. Gnade, *J. Appl. Phys*., 1996, **79**, 7983.
64 B. Balamurugan, B. Mehta, D. Avasthi, F. Singh, A. Arora, M. Rajalakshmi, G. Raghavan, A. Tyagi and S. Shivaprasad, *J. Appl. Phys*., 2002, **92**, 3304.
65 J. Jung, T. Kim, M. Song, Y. Kim and K. Yoo, *J. Appl. Phys*., 2007, **101**, 093708-1.
66 K. Santra, C. K. Sarkar, M. K. Mukherjee, and B. Gosh, *Thin Solid Films*, 1992, **213,** 226.
67 M. Kaur, K. P. Muthe, S. K. Despande, S. Choudhury, J. B. Singh, N. Verma, S. K. Gupta, and J. V. Yakhmi, *J.Crystal Growth*, 2006, **289,** 670.
68 B. J. Hansen, G. Lu, and J. Chen, *Journal of Nanomaterials*, 2008, Article ID 830474.
69 H. Wang, J. Z. Xu, J. J. Zhu, and H. Y. Chen, *J.Crystal Growth*, 2002, **244,** 88.
70 H. H. Lin, C. Y. Wang, H. C. Shih, J. M. Chen and C. T. Hsieh, *J. Appl. Phys.*, 2004, **95**, 5889.
71 F. P. Koffyberg, and F. A. Benko, *J. Appl. Phys.*, 1982, **53**, 1173.
72 W. U. Dangxin, Z. Qiming, and T. Meng, *Phys. Rev. B*, 2006, **73,** 235206.
73 M. A. M. Jaskari, *Modelling Simul Mater. Sci. Eng.*, 2006, **14**, 207.
74 C. Carel, M. M. Bahout, and J. Gaudé, *Solid State Ionics*, 1999, **117,** 47.
75 M. Outokesh, M. Hosseinpour, S. Ahmadi, T. Mousavand, S. Sadjadi and W. Soltanian, *Ind. Eng. Chem. Res*., 2011, **50**, 3540.
76 W. Zhang, X. Wen and S. Yang, *Inorg. Chem*., 2003, **42**, 5005.
77 S. Li, H. Zhang, Y. Ji and D. Yang, *Nanotechnology*, 2004, **15**, 1428.
78 Z. Chen, E. Shi, Y. Zheng, W. Li, B. Xiao and J. Zhuang, *J. Cryst. Growth*, 2003, **249**, 294.

---

79 L. McCusker, R. Von Dreele, D. Cox, D. Louer and P. Scardie, *J. Appl. Crystallogr*., 1999, **32**, 36.

80 R. Cheary and A. Coelho, *J. Appl. Crystallogr.*, 1992, **25**, 109.